Applied Physics Letters ARTICLE scitation.org/journal/apl

Ultrafast amplitude modulation for molecular and hemodynamic ultrasound imaging

Cite as: Appl. Phys. Lett. **118**, 244102 (2021); doi: 10.1063/5.0050807
Submitted: 18 March 2021 · Accepted: 20 May 2021 ·
Published Online: 14 June 2021

Claire Rabut,[1] Di Wu,[2] Bill Ling,[1] Zhiyang Jin,[2] Dina Malounda,[1] and Mikhail G. Shapiro[1,a)]

AFFILIATIONS

[1]Division of Chemistry and Chemical Engineering, California Institute of Technology, Pasadena, California 91125, USA
[2]Division of Engineering and Applied Science, California Institute of Technology, Pasadena, California 91125, USA

[a)]Author to whom correspondence should be addressed: mikhail@caltech.edu

ABSTRACT

Ultrasound is playing an emerging role in molecular and cellular imaging thanks to new micro- and nanoscale contrast agents and reporter genes. Acoustic methods for the selective *in vivo* detection of these imaging agents are needed to maximize their impact in biology and medicine. Existing ultrasound pulse sequences use the nonlinearity in contrast agents' response to acoustic pressure to distinguish them from mostly linear tissue scattering. However, such pulse sequences typically scan the sample using focused transmissions, resulting in a limited frame rate and restricted field of view. Meanwhile, existing wide-field scanning techniques based on plane wave transmissions suffer from limited sensitivity or nonlinear artifacts. To overcome these limitations, we introduce an ultrafast nonlinear imaging modality combining amplitude-modulated pulses, multiplane wave transmissions, and selective coherent compounding. This technique achieves contrast imaging sensitivity comparable to much slower gold-standard amplitude modulation sequences and enables the acquisition of larger and deeper fields of view, while providing a much faster imaging framerate of 3.2 kHz. Additionally, it enables simultaneous nonlinear and linear image formation and allows concurrent monitoring of phenomena accessible only at ultrafast framerates, such as blood volume variations. We demonstrate the performance of this ultrafast amplitude modulation technique by imaging gas vesicles, an emerging class of genetically encodable biomolecular contrast agents, in several *in vitro* and *in vivo* contexts. These demonstrations include the rapid discrimination of moving contrast agents and the real-time monitoring of phagolysosomal function in the mouse liver.

Ultrasound imaging enables the assessment of organ anatomy and function with high spatial and temporal resolution (typically $<500\ \mu$m and 10 ms). Recently, ultrasound has gained increasing capabilities for molecular and cellular imaging due to the development of micro- and nanoscale contrast agents and reporter genes capable of targeting specific disease states[1–3] or visualizing cellular processes, such as gene expression and enzyme activity.[4–6] For example, biomolecular contrast agents known as gas vesicles (GVs)[7] can be used to enhance hemodynamic imaging,[8] visualize lysosomal function,[9] become functionalized with binding domains to target specific cells,[10] or expressed heterologously as reporter genes or biosensors in bacteria[4,6] and mammalian cells.[5] GVs comprise a 2-nm-thick protein shell, enclosing a cylindrical compartment of air with a typical diameter of ~85 nm and length of 500 nm.[11] Certain GV types exhibit strongly nonlinear responses to acoustic pressure, manifesting as reversible buckling of their shell,[12–14] which results in nonlinear scattering of ultrasound [Figs. 1(a) and 1(b)]. Contrast agents, such as GVs, can be detected with improved sensitivity and specificity using ultrasound imaging paradigms, such as amplitude modulation (AM). Parabolic amplitude modulation (pAM)[13] and cross-propagating amplitude modulation (xAM)[15] pulse sequences perform line-by-line scans of the media, transmitting triplets of pulses of relative amplitudes 1/2, 1/2, and 1. Despite being well-suited for GV imaging in biological samples, both pAM and xAM are limited by their imaging depth and framerate, preventing the monitoring of fast nonlinear events across the imaging plane. Ideally, nonlinear imaging of contrast agents should cover the entire field of interest, provide deep penetration, produce a fast framerate, and allow the simultaneous acquisition of other information, such as blood flow or tissue motion.

To address these challenges, we introduce ultrafast amplitude modulation (uAM), a nonlinear paradigm inspired by coherent plane wave compounding for very high frame rate ultrasonography.[16] uAM acquires nonlinear images through the coherent summation of ultrasound signals obtained after transmission of successive tilted, amplitude-modulated, plane waves. In general, plane wave imaging enables rapid one-shot coverage of the entire field, and has been

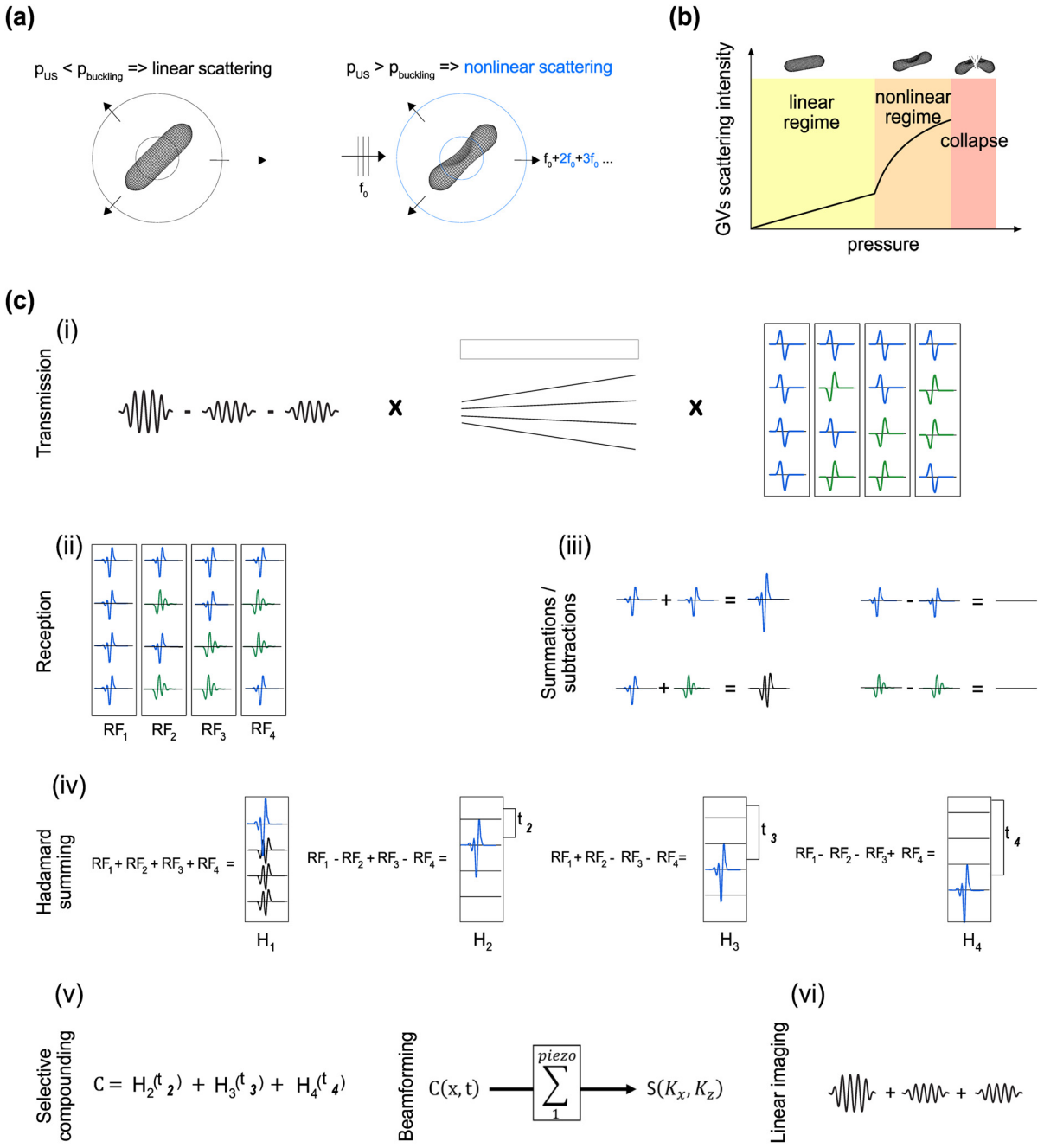

FIG. 1. Nonlinear response of GVs and schematic representation of the uAM pulse sequence with N = 4 angles. (a) The nonlinear scattering behavior of GVs insonified above their buckling pressure enables their detection with AM [adapted from Maresca *et al.*, Phys. Rev. X **8**, 041002 (2018). Copyright 2018 Author(s), licensed under a Creative Commons Attribution (CC BY) license].[15] (b) Schematic scattering intensity curve of GVs as a function of incident pressure. (c) Schematic representation of the uAM pulse sequence for N = 4 angles: (i) AM pulses are combined with MPW transmissions[17] and repeated four times with different polarizations. The polarity combinations are given by the columns of the Hadamard matrix of order 4. (ii) After subtraction of the signals elicited by the two half-amplitude pulses from the full-amplitude one, the nonlinear response appears in the RF data. (iii) The "Hadamard summing" step results in the following combinations: addition of positive nonlinear echoes, subtraction of positive nonlinear echoes, addition of opposite polarity nonlinear echoes and subtraction of negative nonlinear echoes. The results of these combinations are, respectively: a positive echo of amplitude N (N = number of summed echoes), zero, a nonlinear signal, zero. (iv) Following the lines of the Hadamard matrix of order 4, "Hadamard RF" data are obtained where each plane wave is retrieved individually with an amplitude 4. However, H1 also exhibits successive nonlinear echoes. (v) To obtain a final image without nonlinear artifacts, coherent compounding is applied with all the Hadamard RF except H1, and a last beamforming step creates a nonlinear image. (vi) The same acquisition can be used for linear monitoring by summing the contributions of half-amplitude pulses instead of subtracting them.

combined with amplitude modulation to image microbubbles with reduced bubble disruption,[17] However, plane wave pulse sequences typically generate less signal relative to noise per pulse than parabolic or cross-propagating paradigms. The three typical solutions to counterbalance this limitation are increasing the transmit amplitude, increasing the number of compounded angles or averaging multiple sequentially acquired images. However, contrast agents, such as GVs, require imaging within a specific range of pressures [Fig. 1(b)]—typically between 200 kPa (nonlinear regime) and 600 kPa (collapse) for the GV type used in this study,[10] while temporal averaging—by increasing the number of tilted angles or averaging multiple sequential images—leads to a reduced framerate.

To overcome these limitations, uAM combines amplitude modulation with multiplane wave (MPW) transmission and selective coherent compounding. MPW imaging, which comprises the successive transmission of polarized plane waves within a single echo return period, was introduced in 2015 as a means to increase the linear signal-to-noise ratio (SNR) in ultrafast imaging.[18] We endeavored to perform MPW nonlinear imaging by using MPW transmissions with modulated amplitudes. However, because it is based on the recombination of inverted polarity pulses, the Hadamard encoding scheme of MPW transmissions generally requires the assumption of linear scattering, with nonlinear media producing pulse inversion artifacts.[19,20] We hypothesized that we could circumvent this limitation by introducing a new coherent compounding approach that takes selective advantage of a subset of Hadamard sums in which the pulse inversion artifacts are canceled. Moreover, we hypothesized that the ultrafast frames recorded during the resulting AM-adapted MPW acquisitions could be processed for dynamic linear and nonlinear signals, enabling, for example, simultaneous blood flow measurement.[21] In this Letter, we start by describing the ultrasound transmission sequence and signal processing algorithm underlying uAM. Next, we compare the performance of uAM to pAM and xAM in static nonlinear imaging of GVs. We then test the ability of uAM to visualize the motion of flowing GVs in acquisitions lasting a few milliseconds. Finally, we use uAM to image phagolysosomal function in mice, demonstrating the ability to visualize both biomolecular contrast and blood flow simultaneously in a single pulse sequence.

In uAM, bursts of N successive tilted plane waves are repeated three times with modulated amplitude: two bursts of half amplitude (achieved by silencing, respectively, the odd and even elements of the transducer) and one burst of full amplitude. After reception, the subtraction of the two half-amplitude bursts from the full amplitude burst allows the elimination of linear signal and the capture of specifically nonlinear responses [Fig. 1(c-ii)]. On the contrary, the addition of the modulated pulses results in the capture of the linear response. The trios of modulated MPW bursts are then repeated N times, and for each repetition, the polarities of the successive plane waves are given by the column of the Hadamard matrix of order N [Fig. 1(c-i), supplementary material].

In conventional MPW imaging, the contribution of all the Hadamard RF data is summed using appropriate offsets of τ_i to produce a coherent recombination of compounded plane wave signals. We, however, found that the first Hadamard summation systematically leads to a pulse-inversion-like summation of polarized pulses[22] and, therefore, carries inappropriately time-delayed echoes in the recombined signals. This problem is created by nonlinear media, such as contrast agent inclusions, and has been described in.[19,20,23] In addition, we found that all subsequent Hadamard summations do not result in pulse inversion artifacts [Figs. 1(c-ii)–1(c-iv), supplementary material]. To, therefore, benefit from the strength of MPW imaging without creating undesirable nonlinear artifacts due to recombined polarized signals, we introduce *selective coherent compounding* of all Hadamard RF data except the first one (H_1), obtaining a compounded data set C [Fig. 1(c-v)],

$$C = \sum_{i=2}^{N} H_i(t - \tau_i).$$

We then can beamform C by applying a delay-and-sum algorithm and obtain a final nonlinear image S, where harmonic residues at inappropriate time delays resulting from pulse inversion nonlinearity have been eliminated. The resulting image is expected to contain $(N - 1)$ times the signal obtained with a single plane wave. Linear reconstruction similarly benefits from selective compounding with a reduction of nonlinear residues [Fig. 1(c-vi)].

To validate the uAM pulse sequence, we first imaged a 200-μm-diameter cylindrical inclusion of GVs (1 nM) in a 1% agarose phantom [Fig. 2(a)] using four angles (uAM-4) [Fig. 2(b)]. Subtraction of the signals elicited by the two half-amplitude bursts from those received after full-amplitude transmission resulted in backscattered AM echoes along the vertical line crossing the inclusion after each MPW burst [Fig. 2(c)]. After standard Hadamard summation, the sums H_2, H_3, and H_4 each exhibit a single high amplitude echo with an appropriate time delay, but H_1 carries four echoes: the first resulting from the summation of the four in-phase backscattered echoes, and three others resulting from the summing of nonlinear echoes of opposite polarities [Fig. 2(d)]. As a result of this nonlinear artifact, AM images generated by conventional compounding of the Hadamard-RF data show three successive nonlinear residues [Fig. 2(e)]. On the other hand, selective compounding of all the Hadamard sums other than H_1 results in an image showing only the correct GV inclusion [Fig. 2(f)]. These results confirm that the selective compounding approach enables uAM to take advantage of the MPW paradigm without nonlinear Hadamard summation artifacts.

After establishing its basic functionality, we evaluated the performance of uAM with varying angle number [Fig. 3(a)] in comparison with pAM[13] and xAM[15] [Figs. 3(b) and 3(c)] in a tissue-mimicking phantom containing two rows of 2 mm diameter wells filled with GVs. We quantified the contrast-to-tissue ratio (CTR) for both the upper and deeper inclusions $\left(CTR = \frac{|Inclusion - Background|}{\sigma_{Background}}\right)$, as well as the contrast-to-artifact ratio $\left(CAR = \frac{|Upper\ Inclusion - Artifact|}{\text{Artifact}}\right)$ [Fig. 3(d)].

We immediately observe that uAM offers the widest and deepest field of view compared to pAM and xAM. uAM scans the entire imaging plane below the transducer array with each transmission. In contrast, the lateral and depth coverage of pAM are limited by transmission aperture and axial focusing, while xAM is limited by the aperture requirements of cross-propagating waves and the maximal wave intersection depth.[15] In terms of image quality [Fig. 3(e)], the highest CTR values for the upper sample were obtained with xAM, pAM, and uAM-8 and -16 (all around CTR = 15), decreasing substantially for uAM with smaller numbers of angles. The CAR, a measure of resilience to nonlinear propagation artifacts, was best with xAM, which was specifically developed to eliminate such artifacts through cross-propagation.[15] uAM-8 and -16 angles also provided improved

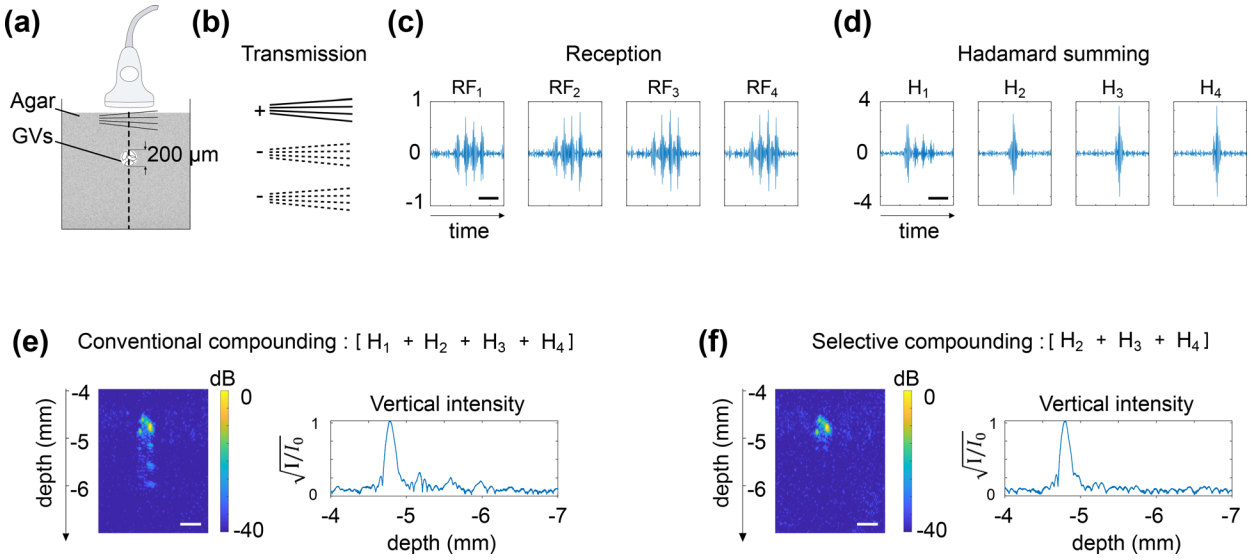

FIG. 2. Selective compounding eliminates the nonlinear artifacts of Hadamard summation. (a) Schematic of an agarose phantom in which a 200 μm diameter inclusion of GVs (1000 pM) is embedded. (b) Transmission sequence and signs of the summation at reception of the AM bursts (N = 4 angles). (c) RF data plotted along the vertical line crossing the inclusion. (d) After Hadamard summing, individual plane waves are retrieved with amplitude N, except for H1, which contains additional nonlinear echoes. (e) Conventional coherent compounding integrates the artifactual nonlinear residues into the final image. (f) Selective compounding omitting H1 enables the reconstruction of a nonlinear image sans artifact. Time scale bars (c.d.): 1 μs. Lateral dimension scale bars (e.f.): 100 μm. Depths calculated from the surface of the probe.

CAR compared to pAM. Finally, the most striking differences in CTR concerned the lower inclusions, which are barely visible in pAM and xAM images, but are robustly seen with uAM, albeit with a lower CTR than the upper row due to attenuation. These results allow us to conclude that uAM with $N_{angles} \geq 8$ offers a wider and deeper field of view than pAM and xAM imaging, comparable near-field CNR, superior CTR at depth, and CAR performance between those of pAM and xAM. 8-angle uAM was selected as the pulse sequence for the remainder of our study.

To compare the lateral and axial resolution of the three AM sequences, we imaged an agar phantom containing sub-wavelength lines of GVs (Fig. S3). This experiment revealed that the lateral resolution in uAM is slightly diminished compared to the classic methods (17% larger than in pAM), while axial resolution is improved (by 50% compared to pAM) [Fig. 3(c)].

Remarkably, the performance improvements described above was obtained while accelerating the imaging frame rate by more than one order of magnitude. For an equivalent 10-mm-deep field, acquiring a pAM or xAM image requires approximately 4 ms, while a uAM-8 image is obtained in just 0.31 ms (supplementary material). To demonstrate the utility of this acceleration, we evaluated the capacity of uAM to visualize flowing GVs *in vitro*. Our experimental setup [Fig. 4(a)] comprised a phantom made of stationary GVs (114 pM) embedded in agarose gel, in which two horizontal tunnels of diameter 1 mm allowed the flow of chosen solutions. A flow of 1 ml/min was created by pump-driven syringes. Comparing xAM [Fig. 4(b)] and uAM [Fig. 4(c)], we first imaged the phantom in which only phosphate-buffered saline (PBS) was flowing through the tunnels. As expected, the tunnels within the effective field of view were devoid of contrast. In xAM, the lower tunnel was obscured by the depth limitation of the sequence, and a strip of higher signal was also evident. We interpret the latter effect as an artifact of the beamforming algorithm, which assumes a uniform supersonic velocity for the plane wave intersection, while boundary effects in the transmitted waves cause imperfect planarity at their ends.

Next, we injected a flow of GVs suspended in PBS at the same concentration as in the gel. Under the same conditions the tunnels blended in with the stationary phantom, making the flowing and stationary GVs indistinguishable in both xAM and uAM. However, in the time it takes to obtain one xAM image, 13 uAM snapshots can be recorded [Fig. 4(d)] and analyzed to create an image specifically of flowing GV using singular value decomposition (SVD)[24] [Figs. 4(e)–4(g)]. This capability to distinguish flowing from stationary nonlinear contrast agents is only possible with the acceleration of uAM.

To examine the utility of uAM *in vivo*, we leveraged its capacity for simultaneous nonlinear and blood flow imaging to visualize mouse liver function. The removal and degradation of circulating particulates by this organ is critical for homeostasis and response to pathogens and serves as a diagnostic marker in common diseases.[25–28] GVs can be used as an intravenous contrast agent to visualize and quantify both phagocytic uptake from the blood and lysosomal degradation by liver macrophages.[9] This paradigm tracks the GV-produced enhancement of vascular contrast with power Doppler (PD) imaging and the uptake and lysosomal degradation of GVs in the liver by AM. In the initial study describing this approach, the liver was imaged with xAM, while the vascular contrast had to be measured separately with linear plane wave imaging. We hypothesized that uAM could simultaneously monitor both the molecular and vascular information in the same organ, providing a more practical diagnostic approach.

To test this concept, we injected GVs intravenously in an anesthetized mouse [Fig. 5(a)] and monitored liver PD and AM signals

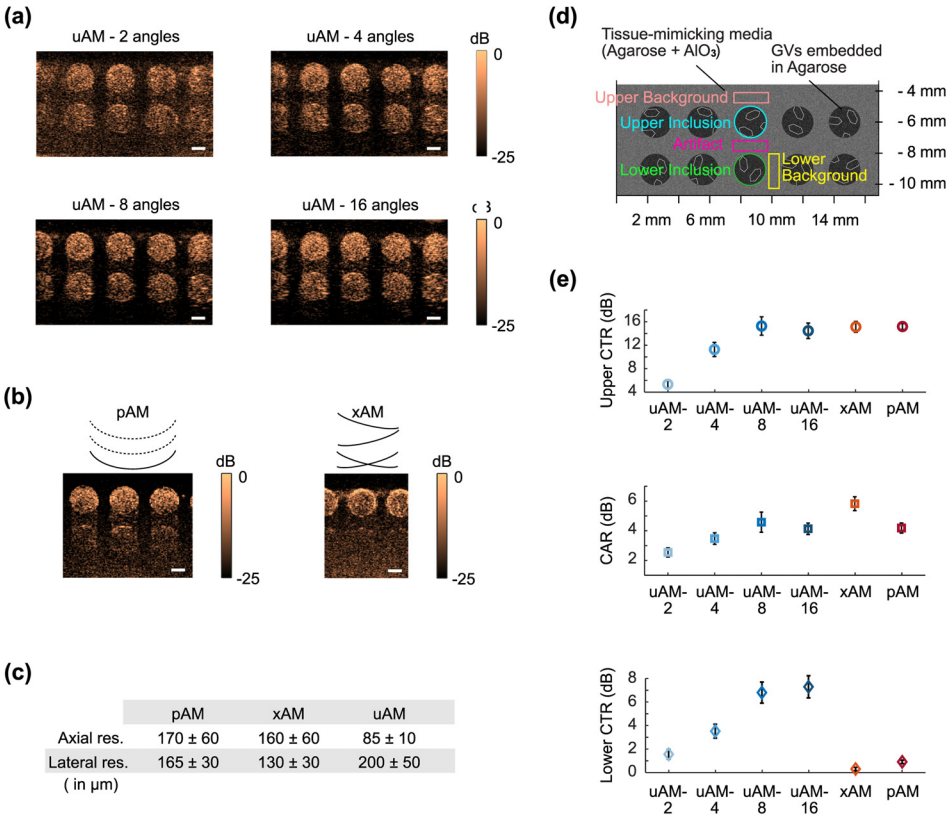

	pAM	xAM	uAM
Axial res.	170 ± 60	160 ± 60	85 ± 10
Lateral res.	165 ± 30	130 ± 30	200 ± 50
(in μm)			

FIG. 3. In vitro evaluation of uAM performance in comparison with pAM and xAM. (a) uAM images of GVs embedded in a tissue-mimicking phantom as a function of the number of tilted angles. (b) Same imaging plane as in (a) acquired with pAM and xAM. (c) Spatial resolution of pAM, xAM, and uAM calculated with an agar phantom containing sub-wavelength lines of GVs. ± represents STD. (d) Schematic of the tissue-mimicking phantom. Quantification was performed on the three middle inclusions of each image over three different sample replicates. (e) Upper CTR, CAR, and lower CTR for each pulse sequence. The upper CTR is evaluated between the upper inclusions and the upper background. The CAR is evaluated between the upper inclusions and the artifact region underneath. The lower CTR is calculated between the lower inclusion and the lower background. Error bars represent ± SEM for N = 3 sample replicates with three wells per replicate. Scale bars: 1 mm.

with a single ultrasound probe and uAM sequence over 2800 s, injecting GVs 800 s after beginning the acquisition. Blocks of 200 uAM images (acquired at 500 Hz) were obtained every 8 s. Leveraging the ability of uAM processing to extract simultaneously both linear and nonlinear information from the same pulse sequence (by summing or subtracting the amplitude-modulated pulses), we processed two complementary sets of data [Fig. 5(b), supplementary material]; by applying a clutter filter[24] to each block of 200 linearly processed uAM image, we obtained PD images of the liver, tracking the vascular enhancement due to circulating GVs;[8] while the nonlinear-processed images from the same plane tracked the contrast of GVs only. AM images, therefore, express the population of circulating GVs, but also GVs taken up by liver tissue. The normalized PD and AM signal time courses [Figs. 5(c) and 5(d)] show that after injection, the vascular signal quickly reaches a maximum within 60 s and then decreases to baseline over 900 s. Meanwhile, the AM signal progressively increases to a maximum around 600 s after the injection, corresponding to the largest concentration of intact GVs in the liver. Macrophages, then, degrade the GVs, resulting in a gradual decrease toward baseline. The recorded blood and liver pharmacokinetics fit a two-compartment model[9] whose rate constants parametrize the concurrent processes of phagocytosis and lysosomal degradation. The apparent uptake rate of $0.402\,\mathrm{min}^{-1}$ and degradation rate of $0.0481\,\mathrm{min}^{-1}$ are within the range expected for healthy mice.[9] This *in vivo* application highlights the capacity of uAM to provide simultaneous access to nonlinear contrast and ultrafast phenomena, such as blood flow.

Our results demonstrate that the implemented ultrafast pulse sequence uAM enables the nonlinear imaging of acoustic contrast agents, such as GVs, with a substantially expanded field of view and dramatically accelerated frame rate compared to existing AM approaches. In addition, it provides simultaneous ultrafast linear acquisition to monitor physiological events, such as blood flow. To achieve this remarkable performance, uAM combines amplitude-modulated transmissions with ultrafast MPW imaging and selective coherent compounding of Hadamard-coded echoes. We anticipate that these performance characteristics will make uAM a method of choice for a wide variety of contrast imaging applications. In particular, uAM will facilitate the development of biomolecular contrast agents, reporter genes, and biosensors for ultrasound by allowing them track dynamic biological events, such as gene expression and enzyme activity, across large fields of view and keep up with rapid signaling phenomena. At the same time, the ultrafast linear capabilities of uAM will allow molecular contrast to be visualized within the context of anatomy and physiology, including the blood dynamics imaged in this study, or the motion-tracking of tissue in ultrasound elastography.[29]

As with any technique, uAM has some limitations. First, the cumulative propagation of plane waves through nonlinear media can lead to artifacts below nonlinear contrast sources. In scenarios where this is a particular concern, xAM currently provides the best artifact cancelation. Second, MPW transmission creates a small dark zone in the near field of the transducer due to the time required to emit a pulse burst. With 8 angles, this dark zone has a depth of approximately

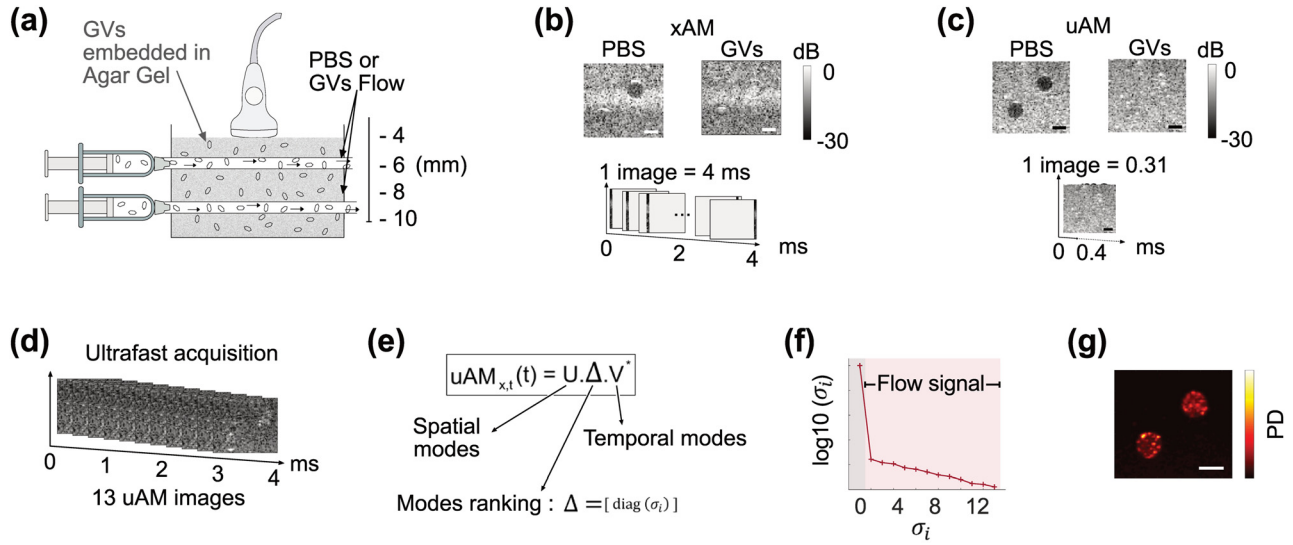

FIG. 4. Ultrafast imaging of GV flows in a nonlinear phantom. (a) Illustration of the flow phantom with two horizontal tunnels of diameter 1 mm allowing controlled flow of PBS or GVs (114 pM) through an agarose gel phantom containing embedded GVs (114 pM). (b) xAM acquisition of PBS and GV flow conditions. One image of 128 vertical lines is acquired in 4 ms. (c) It takes 0.31 ms to acquire a similar uAM image. (d) In 4 ms, 13 uAM images can be acquired. (e) SVD decomposes the 4 ms uAM acquisition of GV flow into a product of separable spatial (U) and temporal (V) matrices weighted by a diagonal matrix Δ. (f) The eigenvalues σ_i of Δ rank the spatial and temporal modes in the data. A high σ_i value is associated with stationary background signal, whereas the lowest σ_i values are associated with flow. (g) Excluding the first SVD mode leads to a power Doppler (PD) image of the GVs flows. Scale bar: 1 mm.

2 mm. In addition, because the half-amplitude plane waves are created in uAM by emitting ultrasound energy with half of the transducer elements, the formation of an acoustic field equivalent of half of the acoustic field created by all the elements requires a longer interference distance after emission. This distance, defined as the near field distance in uAM, was found to be 2.6 mm (at 15 MHz, 0.1 mm pitch) (supplementary material, Fig. S4). Finally, potential memory effects in nonlinear objects under successive excitations[23] were not taken into account in our study as the measured CAR performance was largely satisfying for our application. If such effects arise in future studies, they could be tackled by implementing orthogonal decoding and pulse-inversion-based harmonic suppression.[23] Despite these limitations, uAM's exceptional combination of speed, sensitivity, and spatial coverage will give this pulse sequence a bright future in contrast ultrasound.

See the supplementary material for Material and Methods section describing the detailed pulse sequence, the RF data processing, and the different image processing. See the supplementary figures for details

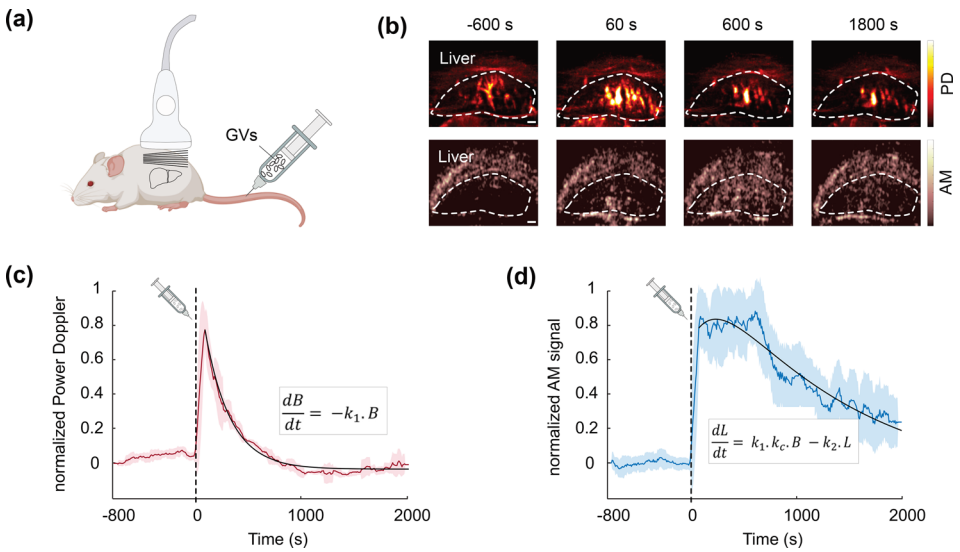

FIG. 5. uAM imaging of phagolysosomal function. (a) Schematic representation of the mouse experiment: purified GVs (100 μl, 3 nM) were intravenously injected in an anesthetized mouse, and the liver was continuously monitored with uAM. Blocks of 200 uAM images were acquired every 8 s. (b) Four time points of PD and AM images acquired simultaneously with uAM. The liver is outlined. Scale bar: 1 mm. (c) Normalized liver PD time. (d) Normalized liver AM time course. Dashed black lines: time of GV injection. Continuous colored lines: mean time course averaged over ±5 neighboring time points (sliding window). Shaded areas: ± STD of neighboring ± 5 time points. Continuous black lines: curves fitted to the data using a pharmacokinetic model where B is the blood signal, L is the liver signal, k_1 is the uptake rate, k_2 is the degradation rate, k_c is a signal scaling factor.

concerning the delay-law of the pulse sequence, the monitoring of nonlinear power Doppler in the *in vivo* application, the spatial resolution set-up, and the near-field distance calculation.

AUTHORS' CONTRIBUTIONS

C.R. and M.G.S. conceived the study. C.R. developed sequence acquisitions and acquired data. C.R. and D.W. developed the processing model. D.M. produced the GVs. Z.J. helped conceiving the dynamic *in vitro* study. B.L. assisted with the *in vivo* study. C.R. and M.G.S wrote the first draft of the manuscript. All authors edited and approved the final version of the manuscript.

This research is supported by the National Institutes of Health (No. R01-EB018975). C.R. is supported by the Human Frontier Science Program (Grant No. LT000217/2020-C). Related research in the Shapiro laboratory is supported by the Chan Zuckerberg Initiative, the Pew Charitable Trust, the David and Lucile Packard Foundation and the Heritage Medical Research Institute.

DATA AVAILABILITY

The data that support the findings of this study as well as the scripts to process the data are openly available in GitHub at https://github.com/ClaireRabut/Rabut_2021_uAM_processing_and_data, Ref. 30.

REFERENCES

[1]A. d. Leon, R. Perera, C. Hernandez, M. Cooley, O. Jung, S. Jeganathan, E. Abenojar, G. Fishbein, A. Jafari Sojahrood, C. C. Emerson, P. L. Stewart, M. C. Kolios, and A. A. Exner, "Contrast enhanced ultrasound imaging by nature-inspired ultrastable echogenic nanobubbles," Nanoscale **11**(33), 15647–15658 (2019).
[2]V. Paefgen, D. Doleschel, and F. Kiessling, "Evolution of contrast agents for ultrasound imaging and ultrasound-mediated drug delivery," Front. Pharmacol. **6**, 197 (2015).
[3]P. S. Sheeran, S. H. Luois, L. B. Mullin, T. O. Matsunaga, and P. A. Dayton, "Design of ultrasonically-activatable nanoparticles using low boiling point perfluorocarbons," Biomaterials **33**(11), 3262–3269 (2012).
[4]R. W. Bourdeau, A. Lee-Gosselin, A. Lakshmanan, A. Farhadi, S. R. Kumar, S. P. Nety, and M. G. Shapiro, "Acoustic reporter genes for noninvasive imaging of microorganisms in mammalian hosts," Nature **553**(7686), 86–90 (2018).
[5]A. Farhadi, G. H. Ho, D. P. Sawyer, R. W. Bourdeau, and M. G. Shapiro, "Ultrasound imaging of gene expression in mammalian cells," Science **365**(6460), 1469–1475 (2019).
[6]A. Lakshmanan, Z. Jin, S. P. Nety, D. P. Sawyer, A. Lee-Gosselin, D. Malounda, M. B. Swift, D. Maresca, and M. G. Shapiro, "Acoustic biosensors for ultrasound imaging of enzyme activity," Nat. Chem. Biol. **16**(9), 988–996 (2020).
[7]M. G. Shapiro, P. W. Goodwill, A. Neogy, M. Yin, F. S. Foster, D. V. Schaffer, and S. M. Conolly, "Biogenic gas nanostructures as ultrasonic molecular reporters," Nat. Nanotechnol. **9**(4), 311–316 (2014).
[8]D. Maresca, T. Payen, A. Lee-Gosselin, B. Ling, D. Malounda, C. Demené, M. Tanter, and M. G. Shapiro, "Acoustic biomolecules enhance hemodynamic functional ultrasound imaging of neural activity," NeuroImage **209**, 116467 (2020).
[9]B. Ling, J. Lee, D. Maresca, A. Lee-Gosselin, D. Malounda, M. B. Swift, and M. G. Shapiro, "Biomolecular ultrasound imaging of phagolysosomal function," ACS Nano **14**, 12210 (2020).
[10]A. Lakshmanan, A. Farhadi, S. P. Nety, A. Lee-Gosselin, R. W. Bourdeau, D. Maresca, and M. G. Shapiro, "Molecular engineering of acoustic protein nanostructures," ACS Nano **10**(8), 7314–7322 (2016).
[11]P. Dutka, D. Malounda, L. A. Metskas, S. Chen, R. C. Hurt, G. J. Lu, G. J. Jensen, and M. G. Shapiro, "Measuring gas vesicle dimensions by electron microscopy," Protein Science **30**(5), 1081–1086 (2021).
[12]E. Cherin, J. M. Melis, R. W. Bourdeau, M. Yin, D. M. Kochmann, F. S. Foster, and M. G. Shapiro, "Acoustic behavior of halobacterium salinarum gas vesicles in the high-frequency range: Experiments and modeling," Ultrasound Med. Biol. **43**(5), 1016–1030 (2017).
[13]D. Maresca, A. Lakshmanan, A. Lee-Gosselin, J. M. Melis, Y.-L. Ni, R. W. Bourdeau, D. M. Kochmann, and M. G. Shapiro, "Nonlinear ultrasound imaging of nanoscale acoustic biomolecules," Appl. Phys. Lett. **110**(7), 073704 (2017).
[14]S. Zhang, A. Huang, A. Bar-Zion, J. Wang, O. V. Mena, M. G. Shapiro, and J. Friend, "The vibration behavior of sub-micrometer gas vesicles in response to acoustic excitation determined via laser doppler vibrometry," Adv. Funct. Mater. **30**(13), 2000239 (2020).
[15]D. Maresca, D. P. Sawyer, G. Renaud, A. Lee-Gosselin, and M. G. Shapiro, "Nonlinear X-wave ultrasound imaging of acoustic biomolecules," Phys. Rev. X **8**(4), 041002 (2018).
[16]G. Montaldo, M. Tanter, J. Bercoff, N. Benech, and M. Fink, "Coherent plane-wave compounding for very high frame rate ultrasonography and transient elastography," IEEE Trans. Ultrason., Ferroelect., Freq. Contr. **56**(3), 489–506 (2009).
[17]O. Couture, M. Fink, and M. Tanter, "Ultrasound Contrast Plane Wave Imaging," IEEE Trans Ultrason Ferroelectr Freq Control **59**(12), 2676–2683 (2012). https://doi.org/
[18]E. Tiran, T. Deffieux, M. Correia, D. Maresca, B.-F. Osmanski, L.-A. Sieu, A. Bergel, I. Cohen, M. Pernot, and M. Tanter, "Multiplane wave imaging increases signal-to-noise ratio in ultrafast ultrasound imaging," Phys. Med. Biol. **60**(21), 8549–8566 (2015).
[19]P. Gong, P. Song, and S. Chen, "Improved contrast-enhanced ultrasound imaging with multiplane wave imaging," IEEE Trans. Ultrason., Ferroelectr., Freq. Control **65**(2), 178–187 (2018).
[20]P. Gong, P. Song, and S. Chen, "Delay-encoded harmonic imaging (DE-HI) in multiplane-wave compounding," IEEE Trans. Med. Imaging **36**(4), 952–959 (2017).
[21]E. Mace, G. Montaldo, B.-F. Osmanski, I. Cohen, M. Fink, and M. Tanter, "Functional ultrasound imaging of the brain: Theory and basic principles," IEEE Trans. Ultrason., Ferroelectr., Freq. Control **60**(3), 492–506 (2013).
[22]C.-C. Shen and P.-C. Li, "Pulse-inversion-based fundamental imaging for contrast detection," IEEE Trans. Ultrason., Ferroelectr., Freq. Control **50**(9), 1124–1133 (2003).
[23]C.-C. Shen and J.-H. Yan, "High-order hadamard-encoded transmission for tissue background suppression in ultrasound contrast imaging: memory effect and decoding schemes," IEEE Trans. Ultrason., Ferroelectr., Freq. Control **66**(1), 26–37 (2019).
[24]C. Demene, T. Deffieux, M. Pernot, B.-F. Osmanski, V. Biran, J.-L. Gennisson, L.-A. Sieu, A. Bergel, S. Franqui, J.-M. Correas, I. Cohen, O. Baud, and M. Tanter, "Spatiotemporal clutter filtering of ultrafast ultrasound data highly increases Doppler and fUltrasound sensitivity," IEEE Trans. Med. Imaging **34**(11), 2271–2285 (2015).
[25]M. L. Block, L. Zecca, and J.-S. Hong, "Microglia-mediated neurotoxicity: Uncovering the molecular mechanisms," Nat. Rev. Neurosci. **8**(1), 57–69 (2007).
[26]C. Wang, H. Yue, Z. Hu, Y. Shen, J. Ma, J. Li, X.-D. Wang, L. Wang, B. Sun, P. Shi, L. Wang, and Y. Gu, "Microglia mediate forgetting via complement-dependent synaptic elimination," Science **367**(6478), 688–694 (2020).
[27]K. Kazankov, S. M. D. Jørgensen, K. L. Thomsen, H. J. Møller, H. Vilstrup, J. George, D. Schuppan, and H. Grønbæk, "The role of macrophages in nonalcoholic fatty liver disease and nonalcoholic steatohepatitis," Nat. Rev. Gastroenterol. Hepatol. **16**(3), 145–159 (2019).
[28]M. G. Netea, F. Balkwill, M. Chonchol, F. Cominelli, M. Y. Donath, E. J. Giamarellos-Bourboulis, D. Golenbock, M. S. Gresnigt, M. T. Heneka, H. M. Hoffman, R. Hotchkiss, L. A. B. Joosten, D. L. Kastner, M. Korte, E. Latz, P. Libby, T. Mandrup-Poulsen, A. Mantovani, K. H. G. Mills, K. L. Nowak, L. A. O'Neill, P. Pickkers, T. van der Poll, P. M. Ridker, J. Schalkwijk, D. A. Schwartz, B. Siegmund, C. J. Steer, H. Tilg, J. W. M. van der Meer, F. L. van de Veerdonk, and C. A. Dinarello, "A guiding map for inflammation," Nat. Immunol. **18**(8), 826–831 (2017).
[29]J.-L. Gennisson, T. Deffieux, M. Fink, and M. Tanter, "Ultrasound elastography: Principles and techniques," Diagnostic and Interventional Imaging **94**(5), 487–495 (2013).
[30]C. Rabut (2021). "Rabut_2021_uAM_processing_and_data," GitHub. https://github.com/ClaireRabut/Rabut_2021_uAM_ processing_and_data